Volume 11
Number 2
14 January 2023
Pages 331–760

Journal of Materials Chemistry C

Materials for optical, magnetic and electronic devices

rsc.li/materials-c

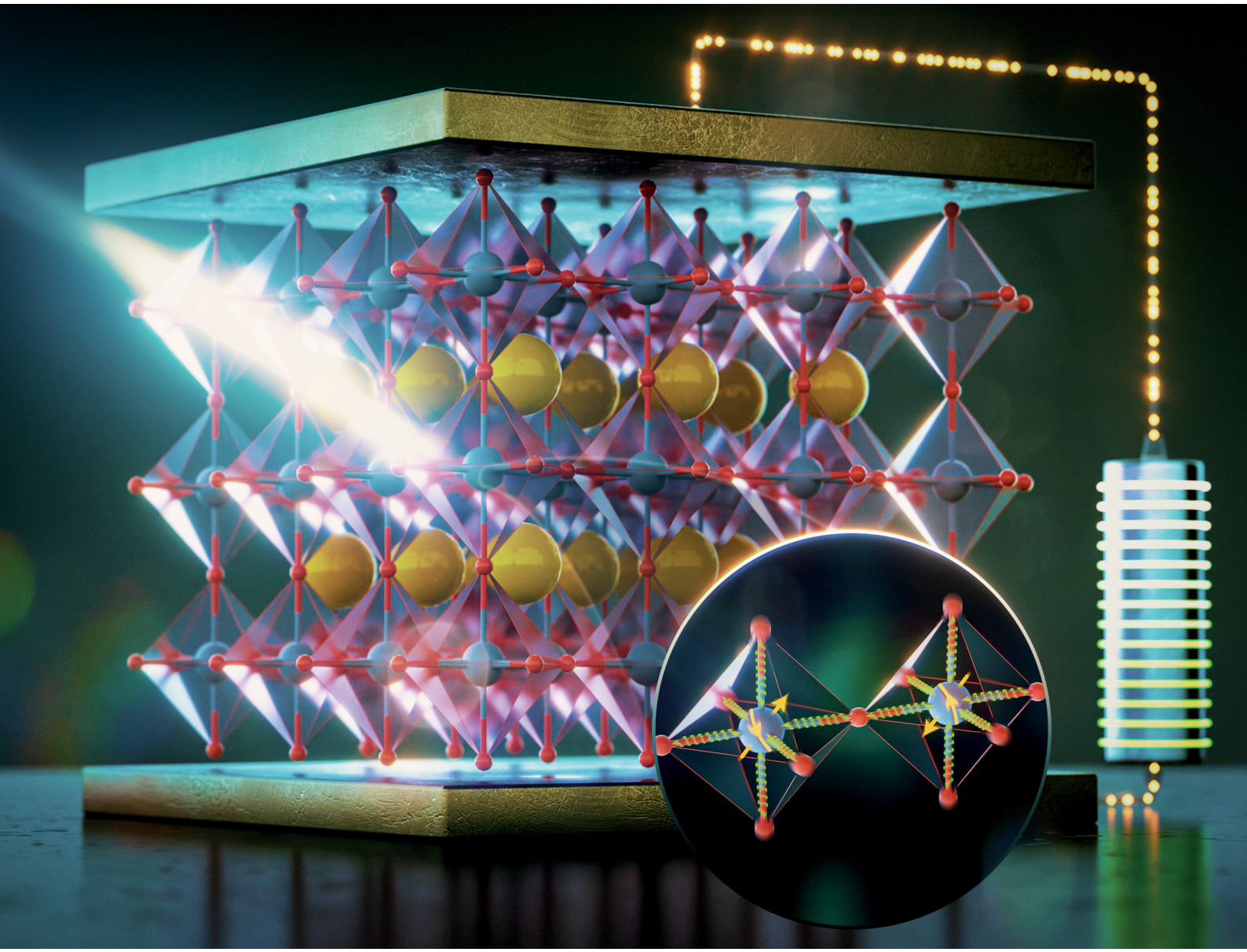

ISSN 2050-7526

ROYAL SOCIETY OF CHEMISTRY

PAPER

J. E. Rodrigues, J. A. Alonso *et al.*
EXAFS evidence for the spin–phonon coupling in the monoclinic $PrNiO_3$ nickelate perovskite

10 YEARS ANNIVERSARY

Journal of Materials Chemistry C

ROYAL SOCIETY OF CHEMISTRY

PAPER

View Article Online
View Journal | View Issue

Cite this: J. Mater. Chem. C, 2023, 11, 462

EXAFS evidence for the spin–phonon coupling in the monoclinic $PrNiO_3$ nickelate perovskite†

J. E. Rodrigues, *[a] A. D. Rosa, [a] J. López-Sánchez, [bc] E. Sebastiani-Tofano,[bc] N. M. Nemes, [d] J. L. Martínez, [b] J. A. Alonso *[b] and O. Mathon[a]

An understanding of the electronic and structural changes across the temperature-induced phase transition in nickelates with a perovskite structure ($RNiO_3$, with R being Y, Tl, rare-earths) is of key importance to shape these materials as devices for industrial applications in several fields, ranging from sensors, catalysts, and non-volatile memory devices. Particularly, $PrNiO_3$ has received special attention because structural, electronic, and magnetic transitions coincide in this compound at temperatures of 125–130 K, which occur under differing pressure and temperature conditions in other nickelates. To draw a refined picture of the origin of these transitions, we investigated the structural changes taking place at a short-range order (local level) in $PrNiO_3$ around the Ni atoms by means of X-ray absorption spectroscopy and at temperatures between 10 and 300 K. Ni K-edge extended X-ray-absorption fine structure (EXAFS) data below $T_N \approx 130$ K confirm the monoclinic phase ($P2_1/n$). At higher temperatures, we observed the convergence of the pair-unit distances Ni–Pr, suggesting the stabilization of the orthorhombic lattice ($Pbnm$). We derived the Einstein temperatures from the temperature-dependent EXAFS data, which provided an estimate of the Ni–O bond stiffness. We found an anomalous behaviour of the Debye–Waller factors σ_Γ^2 of the Ni–O bond below the structural transition at 130 K. The anomalous temperature evolution of σ_Γ^2 was modelled using a molecular field approximation for the scalar spin correlation function for the pair-bond Ni–O. This model suggests strong spin–phonon coupling and the softening of the lattice vibrations below $T_N \approx 130$ K in agreement with the magnetic and vibrational properties of this structure. The present results demonstrate that EXAFS is not only a powerful technique for depicting structural changes, but also for exploring the coupling behaviour between the spin configuration and phonons. The present approach provides new opportunities for such types of studies in related materials.

Received 21st July 2022,
Accepted 17th November 2022

DOI: 10.1039/d2tc03063b

rsc.li/materials-c

Introduction

Nickelates with a $RNiO_3$ perovskite structure (R = Y, Tl, rare-earth elements) undergo an important insulator–metal transition (IMT), which can be easily tuned by temperature, external pressure, and the R cation radius size.[1] The origin and systematics of this transition remain, however, highly debated despite its importance for fine-tuning their properties for industrial applications.[2–5] While there is a general consensus that the bandgap closure mechanism involves orbital overlapping between adjacent Ni and O ions, the involvement of the R cation orbitals remains less constrained.[6,7] Detailed information on the structural and concomitant electronic changes occurring during this transition is required, but is presently only available for a restricted amount of R cations. In this work, we have investigated the atomic and electronic rearrangements in $PrNiO_3$ as a function of temperature across the structural transition temperature. $PrNiO_3$ represents a special case in the group of nickelates: while it has strongly correlated 4f electrons, its R cation radius is intermediate between small- and medium-sized cations (*e.g.* R = Y and La). Besides, its structural phase transition, insulator–metal transition (T_{IM}), and antiferromagnetic ordering (T_N) temperatures coincide at 125–130 K.[8] Therefore, understanding the behaviour of $PrNiO_3$ allows identifying better systematic changes in the properties of nickelates over a wide range of R cation radii.

Previous studies have proposed that the properties and the critical temperature of the insulator–metal transition in nickelates are directly affected by the cation size.[1] For instance, $LaNiO_3$ is metallic under ambient conditions because of its

[a] European Synchrotron Radiation Facility (ESRF), 71 Avenue des Martyrs, 38000 Grenoble, France. E-mail: rodrigues.joaoelias@gmail.com, rodrigues.joaoelias@esrf.fr
[b] Instituto de Ciencia de Materiales de Madrid (ICMM), CSIC, Sor Juana Inés de la Cruz 3, E-28049 Madrid, Spain. E-mail: ja.alonso@icmm.csic.es
[c] Spanish CRG BM25-SpLine at the ESRF, 71 Avenue des Martyrs, 38000 Grenoble, France
[d] Departamento Física de Materiales, Universidad Complutense de Madrid, E-28040 Madrid, Spain

† Electronic supplementary information (ESI) available. See DOI: https://doi.org/10.1039/d2tc03063b

large R, forming a rhombohedral atomic structure ($R\bar{3}c$) that inhibits the insulating and antiferromagnetic state at low temperature. This contrasts with $YNiO_3$ that has an insulating state with a highly distorted monoclinic lattice ($P2_1/n$) under ambient conditions due to the smaller cation size.[9] Upon heating, $YNiO_3$ metallizes at 600 K and transforms into the orthorhombic phase (*Pbnm*). In $YNiO_3$, a rhombohedral phase similar to $LaNiO_3$ was never detected. Instead, $YNiO_3$ undergoes an antiferromagnetic ordering transition at around 143 K (T_N) with a charge ordering between $Ni^{3+\delta}$ and $Ni^{3-\delta}$. The itinerant behavior of the medium-sized rare-earths (R = Nd–Er and $Nd_{0.7}La_{0.3}$) falls between those of $LaNiO_3$ and $YNiO_3$. These medium-size R cation nickelates also exhibit the antiferromagnetic ordering state at low temperature. Studying the electronic and structural transitions occurring in R = Pr could, therefore, link the properties of the small and medium-size R cation nickelates and may allow establishing a refined picture of the systematic property changes as a function of R cation size.

So far, only a few studies have evaluated the atomic and electronic changes in $PrNiO_3$ across the IMT at low temperature and ambient pressure and, therefore, large discrepancies remain on the proposed mechanisms. For example, Piamonteze *et al.* proposed that the insulating state in $PrNiO_3$ is characterized by the local distortions of the [NiO_6] octahedra based on one extended X-ray absorption fine structure (EXAFS) datum acquisition at 8 K.[10] Acosta-Alejandro *et al.* suggested that the insulating low temperature state is due to an inhomogeneous local-atomic structure based on the X-ray absorption near edge structure (XANES) data across the structural phase transition.[11] Both results were later enlightened by the high-resolution neutron diffraction results, demonstrating the occurrence of the monoclinic phase $P2_1/n$ below 130 K. The latter confirmed the long-range charge ordering between $Ni^{3+\delta}$ and $Ni^{3-\delta}$, as so-called charge disproportionation at the Ni sites.[8] The magnetic transition has been so far only studied by neutron diffraction, showing that the magnetic moment abruptly decreases above T_N. However, the mechanism has only been investigated in related systems, such as the $LaMnO_3$ manganites using Raman spectroscopy that suggested a potential effect of the spin–phonon coupling.[12] In this compound, the IMT is absent leaving the question if the spins couple with the lattice also in the $PrNiO_3$ perovskite.

Despite these achievements, the interplay between the electronic and atomic structural changes behind the insulator–metal transition in $PrNiO_3$ is not fully resolved. Therefore, we monitored the structural and electronic changes across the low temperature-induced structural phase transitions in $PrNiO_3$ using synchrotron X-ray absorption spectroscopy (XAS) at Ni K-edge. Such a technique provides detailed information on both the local-atomic structure and the electronic properties around the absorber atom (Ni).[13] In particular, EXAFS provides detailed insights into the local-atomic scale, such as the pair-bond distances, disorder, and coordination numbers around the absorber.[14] We performed runs to cover the structural phase transition/insulator–metal transition/magnetic ordering in $PrNiO_3$ under vacuum conditions in the temperature range of 10–300 K. Understating the underlying mechanisms for these transitions has a pivotal consequence for further improvements in devices used in different technological or industrial fields, ranging from sensors, catalysts, non-volatile memory devices. Here, we provide a careful analysis of the local-atomic structure in $PrNiO_3$ at the onset of the aforementioned phase transition. Our results show strong evidence for the spin–phonon coupling and the softening of the lattice vibrations below $T_N \approx 130$ K.

Methods

Highly polycrystalline $PrNiO_3$ nickelate was synthesized using the liquid-mixture method.[15] From a solution with metal nitrates in citric acid, a black powder was obtained after a slow decomposition of the formed resin at 600 °C. A thermal treatment at 1000 °C under 200 bars under an O_2 atmosphere was required for the stabilization of the perovskite single phase.

The detailed crystal structure under room conditions of the $PrNiO_3$ powder was then determined from synchrotron X-ray diffraction (SXRD) data at the beamline BM25 of the ESRF. For these measurements, we used an incident X-ray beam with a wavelength of λ = 0.4959 Å. The sample was contained in a quartz capillary of 0.5 mm diameter, which was rotating during data acquisition, in the angular 2θ interval between 5 and 45°, with 0.005° steps. A 2D photon-counting X-ray MAXIPIX detector was employed and the data were processed using the BINoculars software.[16,17] The diffraction pattern was analysed by the Rietveld method, using the Fullprof refinement program.[18] A pseudo-Voigt function generated the profile shape. The refined parameters included unit-cell constants, positional coordinates, and isotropic displacement factors for all the atoms.

The Ni K-edge (at 8.333 keV) XAS run was performed on $PrNiO_3$ aiming to determine the mechanism of the insulator–metal transition/magnetic ordering using EXAFS and was conducted in a temperature interval between 10 and 300 K at the beamline BM23 at the ESRF.[19] For this purpose, a compacted pellet made of a mixture between $PrNiO_3$ and cellulose, in appropriate proportions to achieve an edge jump of about 0.6, was prepared. The pellet was placed inside a liquid He cryostat under vacuum (work pressure: 10^{-7}–10^{-6} mbar). The temperature was monitored using a Pt-based thermocouple placed close to the sample. XAS data at Ni K-edge were acquired using an unfocused beam collimated to 3 × 1 mm^2 using slits. Harmonic rejection was achieved by setting two parallel silicon mirrors with an incident angle of 3 mrad. The ionization chambers filled with an appropriate gas mixture were used to determine the photon intensities before and after the sample. A third ionization was placed to collect the photon flux after a Ni foil, which was considered for monochromator angle-to-energy calibration.

Raw XAS data reductions were conducted using ATHENA software for the pre-edge background subtraction, edge jump normalization, and the extraction of the EXAFS oscillations. Then, the EXAFS analyses were performed using ARTEMIS software, based on FEFF's multiple-scattering path expansion.[20,21] Based on the standard EXAFS equation, the FEFF program provides the amplitude, phase, and mean free path functions.

Fourier-transform (FT) windows in both k- and R-spaces were set to k = 2–13.5 Å^{-1} and R = 1.1–5.9 Å, leading to 42 independent parameters. Seven single scattering paths (Γ_k) up to the fourth shell were considered. Fitted parameters encompassed the average distance and the Debye–Waller factor for each path, while the coordination number was kept fixed as extracted from neutron diffraction data to avoid correlation with the Debye–Waller factor. The amplitude reduction factor S_0^2 was fixed to 0.8053, which was obtained from the fit of the reference Ni foil. A total of 21 parameters were used during the fitting procedure, which includes the background coefficients. The average R-factors of the fittings for all temperature points approached the value of 0.058(4), with an average E_0 correction of $\Delta E \approx -2.5(1.0)$ eV.

Magnetic measurements between 10 and 300 K were performed using a SQUID magnetometer (MPMS-3) from Quantum Design (San Diego, USA) under an applied magnetic field of 100 Oe. The sample was positioned in a residual vacuum under a He atmosphere (pressure of 10^{-5} torr) in the temperature range from 10 up to 300 K.

Results and discussion

The results of this paper are presented as follows: first, a brief crystal structure description under room conditions of the as-obtained $PrNiO_3$ sample is provided. Then, a local structure study across the insulator–metal transition temperature ($T_N \approx 125$ K) is performed using EXAFS data collected in the temperature range of 10–300 K. The results from EXAFS analyses were used to model the Ni–O bond stiffness and the potential of the spin–phonon coupling contributions across the transitions.

Crystal structure at room temperature

The diffraction data of the synthetic $PrNiO_3$ sample acquired at room temperature (RT, 295 K) are represented in Fig. 1, together with the Rietveld refinement. They confirmed that the sample is mainly composed of $PrNiO_3$ in the orthorhombic structure, as defined in the space group *Pbnm* (S.G. #62). In this structure, Pr is located at the low symmetry Wyckoff 4c (x, y, 1/4) sites; Ni atoms occupy a high-symmetry site at 4b (1/2, 0, 0), while two oxygen atoms exist including O1 and O2 that are located at low symmetry sites 4c and 8b (x, y, z), respectively. From the diffraction data, we have detected a minor impurity of NiO (bustenite; a = 4.146 Å) with a weight percentage of 2.46(4)% wt., which was included in the refinement. The refined unit-cell parameters of $PrNiO_3$ under ambient conditions include a = 5.40337(7) Å, b = 5.36198(7) Å, c = 7.6045(1) Å, and V = 220.323(5) Å^3. They are comparable with those described in the literature (*e.g.* a = 5.4161(5) Å, b = 5.3737(5) Å, c = 7.6226(7) Å; V = 221.85 Å^3). In Fig. 1a the raw and fitted SXRD data together with the goodness of the fit is shown. In Fig. 1b a schematic view of the crystal structure is presented highlighting the slight tilting of the [NiO_6] octahedra network in the orthorhombic structure along the c-axis.

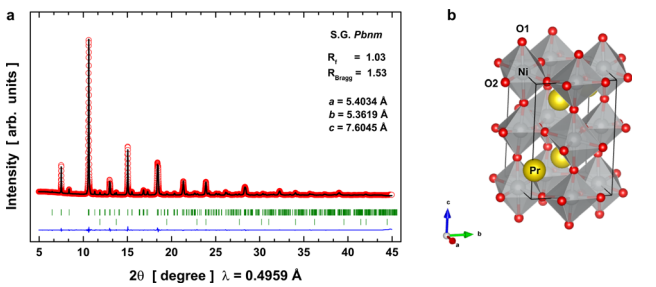

Fig. 1 SXRD data refinement and crystal structure of $PrNiO_3$ at room temperature. (a) Rietveld plot: observed (red circles) and calculated (black line) synchrotron X-ray diffraction pattern for $PrNiO_3$ at 295 K shown together with expected peak positions (green line underneath the pattern) and the fit residual (blue line at the bottom). The second series of Bragg ticks correspond to the expected peak positions of NiO, which is present as a minor phase. (b) Crystal structure of orthorhombic $PrNiO_3$: oxygen, nickel, and praseodymium ions are given in red, silver, and yellow, respectively.

Evolution of the local structural environment across the IMT

EXAFS data were acquired up to 16 Å^{-1} in the k-space and across the structural transition at 130 K using a liquid–helium cryostat. This spectral dataset was used to monitor the local structure around the Ni absorber in $PrNiO_3$ and the temperature evolution of the pair-bond distances (R_Γ) and their associated Debye–Waller factors (σ_Γ^2; or mean-square relative displacements, MSRDs) across the structural phase transition from $P2_1/n \rightarrow Pbnm$ beyond the Ni–O bonds. In the case of $PrNiO_3$, this structural transition coincides with both insulator–metal and magnetic ordering transitions in the phase diagram.[6] For fitting the EXAFS spectra, seven scattering paths were used by setting both k and R ranges to Δk = 11.5 Å^{-1} and ΔR = 4.8 Å, respectively. Details of the fitted parameters from the EXAFS data of $PrNiO_3$ at 10 K are listed and compared with neutron diffraction data in Table 1, showing a reasonable agreement. In Fig. 2a, the experimental and fitted EXAFS oscillations [$\chi(k)$] at 10 K are shown together with individual oscillations (contributions) from the single scattering paths Γ_k (k = 1–7). In Fig. 2b, both the modulus and real part of the Fourier-transform (FT) oscillations [$\chi(R)$] are represented.

To model the EXAFS signal at 10 K, we started from the monoclinic phase (at 10 K) as the input structural model to generate both single and multiple scattering paths using the FEFF code integrated with the ARTEMIS software package. This provided the amplitude, phase, and mean free path functions for each path used as input parameters in the fitting procedure. At 10 K, monoclinic $PrNiO_3$ is characterized by the charge disproportionation between two Ni octahedra, here referred to as Ni1 and Ni2, corresponding to $Ni^{+3+\delta}$ and $Ni^{+3-\delta}$, respectively. Each of the octahedra exhibits three sets of Ni–O distances (see Fig. S1 of the ESI†). Averaging these three distances reveals that the [$Ni1O_6$] octahedron is smaller compared to [$Ni2O_6$] by 0.071 Å. The EXAFS technique provides the resolving power to study such differences in distances.

Our FEFF calculations reveal that the most intense first peak at 2 Å in the modulus of the Fourier transform function $|\chi(R)|$ results from the contribution of these 6 single-scattering paths (see the ESI† for a detailed explanation). However, including all 6 paths in the model EXAFS model at 10 K (monoclinic phase)

Table 1 Refined parameters from Ni K-edge EXAFS data at 10 K. Abbreviations: R_Γ is the pair-unit distance, N_Γ the average coordination number, ${\sigma_\Gamma}^2$ the Debye–Waller exponent, θ_E the Einstein temperature, ${\sigma_{stat}}^2$ the static disorder, and NPD is neutron diffraction data. Here, the coordination number for each path was kept fixed and its value extracted from NPD data elsewhere[8]

		EXAFS at 10 K			Einstein's model		NPD at 10 K
Attribution	Path	R_Γ [Å]	N_Γ	${\sigma_\Gamma}^2$ [$\times 10^{-3}$ Å^2]	θ_E [K]	${\sigma_{stat}}^2$ [$\times 10^{-3}$ Å^2]	d [Å]
Γ_1	Ni_a–O_{1a}	1.911(2)	2	4.4(3)	553(2)	0.1(1)	1.915–1.921
Γ_2	Ni_a–O_{2a}	1.962(2)	4	4.4(3)	553(2)	0.1(1)	1.961–1.972
Γ_3	Ni_a–Pr_1	3.202(5)	2	3.0(5)	267(3)	0.0	3.149
Γ_4	Ni_a–Pr_2	3.339(5)	2	3.0(5)	267(3)	0.0	3.291–3.343
Γ_5	Ni_a–Pr_3	3.369(5)	2	3.4(5)	278(2)	1.2(5)	3.437
Γ_6	Ni_a–Ni_1	3.921(8)	6	8.0(9)	315(2)	5.4(5)	3.806–3.816
Γ_7	Ni_a–Ni_2	5.44(2)	12	4.3(4)	—	—	5.387–5.411

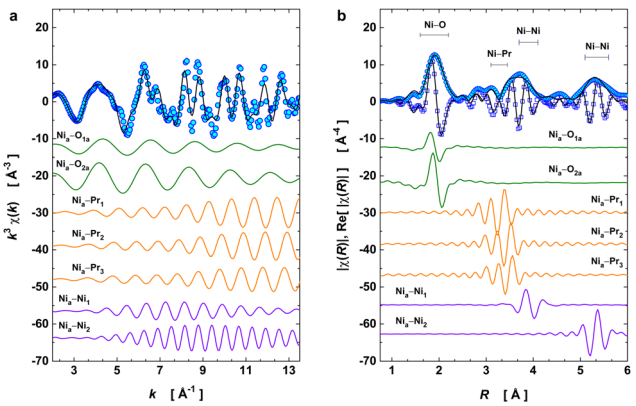

Fig. 2 Ni K-edge EXAFS fitting at 10 K. (a) k^3-weighted oscillation $\chi(k)$. (b) Fourier transform magnitude of $k^3\chi(k)$ and the real part of $\chi(R)$. As shown in figure, the raw EXAFS signal can be reproduced by seven single scattering path contributions, namely: Ni–O (2 Å), Ni–Pr (3.3 Å), Ni–Ni (3.9 Å), and Ni–Ni (5.4 Å). Such a model provides a description of the average octahedral unit [NiO_6], the distorted sublattice of Pr cations, and the lattice distortion along the c-axis (pair-unit Ni_a–Ni_1), while Ni_a–Ni_2 has a path encompassing the edges of the first-Brillouin zone. Experimental data points are represented by open symbols, black solid line denotes the best EXAFS fit. Coloured solid lines discriminate the individual single scattering paths which compose the EXAFS oscillations.

is not reasonable, because this would result in overfitting and, therefore, unreliable results. In general, in EXAFS analysis overlapping distances below 0.01–0.02 Å cannot be resolved, which is due to the limited data range in k- and R-spaces.

To provide a reliable model of Ni–O distances, we considered that the peak at 2 Å is composed of only two sets of averaged Ni–O distances, which will be referred to as Ni_a–O_{1a} and Ni_a–O_{2a} (subscript "a" denoting "average"). The first average distance was obtained from averaging all paths with $R_\Gamma < 1.89$ Å, which are the 4 short Ni_1–$O_{1,3}$ (see Fig. S3 of the ESI†). The second average distance was calculated by averaging the remaining 8 long Ni-distances with $R_\Gamma > 1.89$ Å. To ensure correct weighting of path contributions during fitting, we set the coordination numbers (CN) to 2 and 4 for Ni_a–O_{1a} and Ni_a–O_{2a}, respectively.

These structural input models allow studying the local structural variations due to the charge disproportionation in $PrNiO_3$ below 130 K. This approach partially agrees with that used by Piamonteze *et al.*,[10] which in addition included a third scattering path Ni–O with a pair-distance of 1.82 Å. However, this last path seems to be very short for a Ni–O bond distance, not agreeing with the structural data reported by Medarde *et al.* from neutron diffraction.[8] The fitted path length for Ni_a–O_{1a} reveals a value of 1.911(2) Å, which agrees well with a contribution from the small [$Ni1O_6$] octahedra (Table 1). Finally, we have constrained the paths Ni_a–O_{1a} and Ni_a–O_{2a} (referred to as fitting paths Γ_1 and Γ_2 in Table 1) to have the same Debye–Waller factor, meaning that this parameter describes the average disorder at the level of the [NiO_6] octahedron.

The broad peak at the radial interval of 3.2–3.4 Å was partly ascribed to the pair-units interaction between Ni and Pr, comprising three paths here referred to as Γ_3, Γ_4, and Γ_5. These paths describe the sublattice composed by the R-sites (R = Pr). The lengths and their variations of these paths provide information on the octahedral tilting in $PrNiO_3$,[22] because the tilting process is strongly dependent on the radius of the R element. For instance, previous studies demonstrated a linear behaviour between the quasi-softmodes encompassing the pair-unit R–Ni and the tilt angle of $RNiO_3$.[23] Based on this observation, the temperature evolution of these paths features may be also be used as order parameters for describing structural phase transitions in nickelates. To reduce uncertainties of their fitted parameters, we have included constraints to their Debye–Waller factors following the crystallographic symmetry considerations: the paths Γ_3 and Γ_4 present the same disorder parameter, while path Γ_5 shows an independent disorder exponent for accounting for a fourth pair-unit Ni–Pr that is missing in our model. Attempts to include it in the fitting failed probably due to the high disorder of this scattering path or possible Pr vacancies within the unit cell. Another possibility is that these oscillations are almost out-phase, which hinders a precise characterization of their features.

The contribution of pair-units Ni–Ni at 3.9 and 5.4 Å were included in the fit as paths Γ_6 and Γ_7, respectively. The path Γ_6 is of particular importance because the length of R_6 corresponds to half of the lattice parameter c for the orthorhombic lattice *Pbnm*. Hence, it can provide information about the possible distortions of the lattice and the suppression of the exchange interaction between the Ni magnetic moments within the first-Brillouin zone. For this path, the coordination number was kept equal to 6 with the same Debye–Waller factor. The path Γ_7 encompasses a trajectory to the edges of the first-Brillouin zone, with a reasonable intensity in the Fourier-transform oscillations. For such a path,

we have considered a coordination number fixed to 12 nickel atoms, with the same disorder parameter in each pair-unit Ni_a–Ni_2.

With the model in Table 1, we have evaluated the local structure in $PrNiO_3$ nickelate across the structural phase transition at 125–130 K that has the insulator–metal transition (T_{IM}) and antiferromagnetic ordering transition (T_N) occurring at the same temperature value. For this purpose, XAS spectra of $PrNiO_3$ were recorded from 10 to 300 K with fine temperature steps in the vicinity of the structural transition. Fig. 3 exhibits the k^3-weighted EXAFS oscillations $k^3\chi(k)$ and the moduli of $\chi(R)$ and their real parts Re[$\chi(R)$] at selected temperatures.

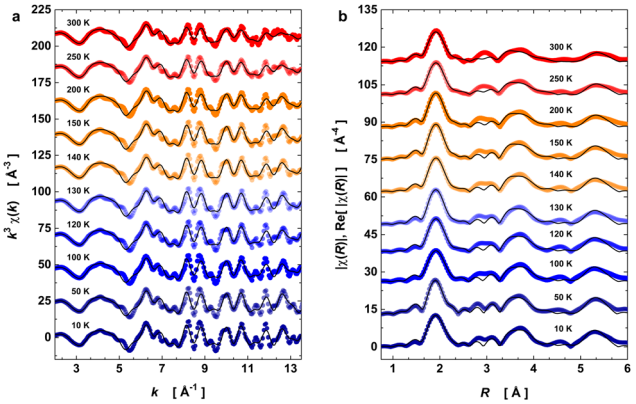

Fig. 3 Temperature-dependent EXAFS data at Ni K-edge. (a) k^3-weighted EXAFS oscillations in k space. (b) Modulus and real part of the Fourier transform oscillations $\chi(R)$ in R space. The open symbols denote the experimental data, whereas solid lines are the best EXAFS fit adjusted. The data acquisition was performed under heating from 10 up to 300 K. The temperature effect on the EXAFS data is visible through the damping of $k^3\chi(k)$ and the peak broadening of $|\chi(R)|$.

The temperature-dependence of the fitted EXAFS parameters extracted from the best spectral fitting are presented in Fig. 4 together with a schematic representation of the scattering paths used for the EXAFS oscillations. We have seen an anomalous trend for the pair-unit distance (R_Γ) and Debye–Waller factor ($\sigma_\Gamma{}^2$) for almost all the studied paths across the structural transition at 125–130 K (*i.e.*, as a departure from the expected Einstein behaviour in black lines). Our results show a slight change in the slope of the average Ni–O bond distance of the [NiO_6] octahedra at 130 K (Fig. 4a) that is concomitant with a drop in the $\sigma_\Gamma{}^2$ values of the first two paths (Fig. 4b). The fact that distances Ni_a–O_{1a} and Ni_a–O_{2a} are almost unaltered across T_{IM} means that the charge disproportionation remains at the local level. At the Ni–Pr sublattice, variations along the R_Γ and $\sigma_\Gamma{}^2$ can also be noticed, as shown in Fig. 4c. The R_Γ values of the three paths accounting for the Ni–Pr sublattice showed a pronounced anomaly at the onset of structural transition. Such an evolution is most obvious for the paths Γ_4 and Γ_5 that approached each other at around 130 K and for temperatures above it. This converges around at the structural transition

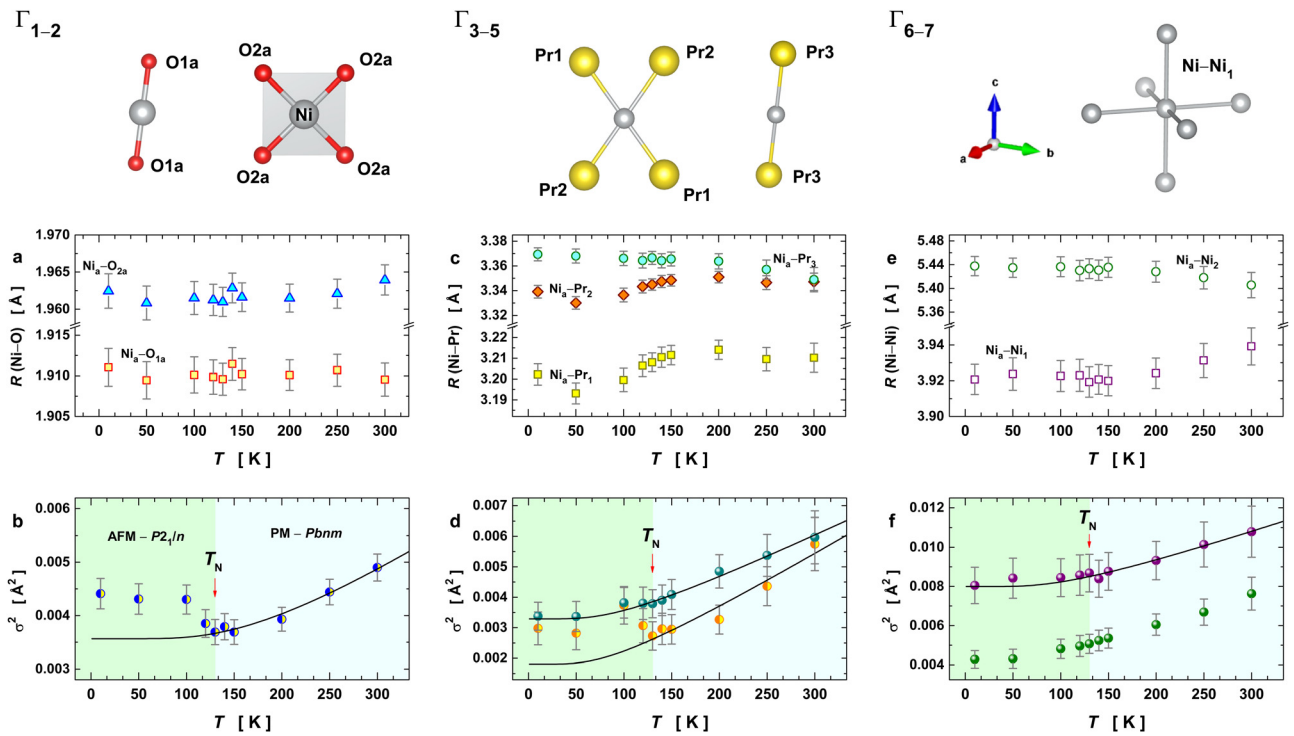

Fig. 4 Temperature dependence of the structural parameters extracted from the fits to the EXAFS data. A schematic representation of the single scattering paths corresponding to the data shown below is given on the top of the figure. Symbols in the individual plots represent EXAFS parameters extracted from the best fit together with their respective error bars, while the black solid lines denote Einstein's model fitting for temperatures above 130 K (a) pair-unit distances Ni_a–O_{1a} and Ni_a–O_{2a} and (b) their Debye–Waller factors (Γ_1 and Γ_2 have the same value for DW). (c) Pair-unit distances Ni_a–Pr_1, Ni_a–Pr_2, and Ni_a–Pr_3 and (d) their Debye–Waller factors (Γ_3 and Γ_4 are described by the same DW, while Γ_5 has an independent DW value). (e) Pair-unit distances Ni_a–Ni_1 and Ni_a–Ni_2 and (f) their Debye–Waller factors.

temperature suggests that the Ni–Pr sublattice becomes more symmetric with partial suppression of the charge ordering between $Ni^{3+\delta}$ and $Ni^{3-\delta}$, taking place only in the monoclinic phase $P2_1/n$ and it is absent in the orthorhombic *Pbnm*.[6,8] The evolution of the Debye–Waller factors with temperature for these three paths Γ_{3-5} are drawn in Fig. 4d. They exhibited a similar but subtler trend to the one seen for the pair-bonds Ni–O. In summary, this indicates that such a transition is accompanied by significant changes in the crystal structure at the local-scale within the unit-cell (<5 Å).

Fig. 4e displays the temperature evolution of the two Ni–Ni cation distances for the paths $\Gamma_{6,7}$ (pairs Ni_a–Ni_1 and Ni_a–Ni_2). The R_Γ values of $\Gamma_{6,7}$ behave almost in an opposite way to each other until 130 K, showing a tendency to converge at higher temperatures. The corresponding Debye–Waller factors and their temperature evolution are depicted in Fig. 4f. They revealed a small anomaly at the structural transition temperature at 130 K. This anomaly lies within the uncertainty of ${\sigma_\Gamma}^2$, making any conclusion about the variation of this parameter unprecise. However, it is evident that the anomalous behaviour of the disorder parameters is more pronounced when the neighbouring shell is closest to the absorber atom (Ni), the case of the paths Γ_1 and Γ_2. Therefore, this anomaly has a local origin that encompasses paths up to the second shell (R_Γ < 3.4 Å) and it could be associated with the local actions of the spin interaction between Ni and its neighbourhood.

Evaluation of bond disorder and vibrational properties in orthorhombic $PrNiO_3$

We used the temperature-dependence of fitted EXAFS parameters to evaluate the lattice dynamics of $PrNiO_3$. It details the dynamic part of the Debye–Waller factor for the paths Γ_k (k = 1–6), which was fitted to Einstein's model, as described below:

$$ {\sigma_\Gamma}^2(T;\theta_E,\sigma_{stat}) = {\sigma_{stat}}^2 + \frac{\hbar^2}{2\mu k_B \theta_E}\coth\left(\frac{\theta_E}{2T}\right) \qquad (1) $$

such that, μ is the reduced mass of the pair-unit (*e.g.* Ni–O, Ni–Pr, and Ni–Ni); ${\sigma_\Gamma}^2$ is the intrinsic (or static) disorder; θ_E is the Einstein temperature; and (k_B, $\hbar$, T) maintain their usual meaning. From eqn (1) the Einstein temperature θ_E, that is an intrinsic property of the pair-bond unit and depends on its bond stiffness, and ${\sigma_{stat}}^2$ at 0 K was extracted from data for the Debye–Waller factor above 130 K. Then, the fitted curve was extrapolated for lower temperatures to highlight the departure of the experimental points below 130 K from Einstein's model. The fitting results are shown as solid black lines in Fig. 4. The approach of Einstein's model is more convenient than that of Debye's model one, because here the pair-units are treated as non-coupled quantum harmonic oscillators.[24,25] Otherwise, the Debye's model is more precise for describing thermal displacements, as extracted from diffraction data, possessing an ordered scale at a long-range which is valid for dozens or hundreds of unit-cells.[14] In the Debye approach, the coupled harmonic oscillators are precise enough to describe the thermal displacements and, then, to provide information about the Debye's temperature and specific heat.

At the onset of the structural phase transition at 130 K and below, a departure from the Einstein-like trend was clearly noticed in Fig. 4b and d for the shells Ni–O ($\Gamma_{1,2}$) and Ni–Pr ($\Gamma_{3,4}$), respectively. For the paths Ni–Pr (Γ_5) and Ni–Ni (Γ_6), it is more difficult to say if this trend really takes place below the transition temperature due to the error bars, see Fig. 4d and f, respectively. Therefore, the fitting of ${\sigma_\Gamma}^2$ using Einstein's model was conducted for temperatures above 130 K and the resulting Einstein temperature of each path is listed in Table 1.

In the following, we compare the extracted Einstein-temperatures for individual paths to known vibrational Raman modes for better understanding the experimental observations. This comparison is based on the nature of the Debye–Waller factor extracted from EXAFS, which represents a mean-square relative atomic displacement along the direction of the scattering path (*i.e.* parallel), being thus connected to some of the vibrational modes of the system. For the orthorhombic $PrNiO_3$, 24 Raman (Γ_{Raman} = $7A_{1g} \oplus 7B_{1g} \oplus 5B_{2g} \oplus 5B_{3g}$) and 25 infrared ($\Gamma_{Infrared}$ = $7B_{1u} \oplus 9B_{2u} \oplus 9B_{3u}$) active phonons are predicted, such that most of them appear as accidental degeneracies or with very low intensities.[7] However, they are assigned as symmetric and asymmetric stretching modes, bending modes, librations (rigid rotations of [NiO_6] units), and translations (Pr movements against the [NiO_6] units), appearing at high down to low-wavenumbers, respectively, in both Raman and infrared spectra.[6,7,26] A direct correlation of the Debye–Waller factor and the vibrational modes by comparing them with the θ_E values has to be done with caution, because ${\sigma_\Gamma}^2$ projects the normal modes along the radial direction (*i.e.* parallel to the scattering path).

In $PrNiO_3$, the translational Raman modes appear in the range of 100–200 cm^{-1}. The paths Ni_a–Pr (Γ_{3-5}) have an θ_E in the range of 185–193 cm^{-1} and therefore they are likely related to the displacements of Pr against Ni. The path Ni_a–Ni (Γ_6) has a θ_E of 315(2) K which could be assigned to some extent to the libration and/or bending Raman mode at 219 cm^{-1}. The paths Ni_a–O_a ($\Gamma_{1,2}$) with θ_E of 553(2) K (385 cm^{-1}) with an intrinsic disorder of 0.1(1) × 10^{-3} $Å^2$ may be linked to the asymmetric stretching of [NiO_6] units. The reasons for that are as follows: (i) the symmetric stretching vibrations of $PrNiO_3$ occur above 400 cm^{-1} and (ii) the uneven path distances are most likely describing the out-of-phase displacements of apical and equatorial oxygens from the Ni absorber.[7]

Bond stiffness of Ni–O and Ni–Pr for orthorhombic $PrNiO_3$

Using the Einstein temperature, an estimate of the bond stiffness from the scattering paths (for the shells Ni–O and Ni–Pr) in orthorhombic $PrNiO_3$ can be obtained from a harmonic approximation that defines an average force constant (κ_E),[27,28] *i.e.*

$$ \kappa_E = \mu\left(\frac{k_B\theta_E}{\hbar}\right)^2 \qquad (2) $$

The estimated force constant for the pair-bond Ni–O is around 6.8(4) eV $Å^{-2}$ (1.1 mdyn $Å^{-1}$), which agrees with typical force constant calculated for bonds M–X (M = Ni, Co, Mn; X = P, O) in

both tetrahedral and octahedral environments.[29,30] The estimation of the force constant for the pair-unit Ni–Pr is less reliable, because this is not a chemical bond as in the case of Ni–O. Regardless of that, the average force constant as calculated by eqn (2) for the pair-unit Ni–Pr lies in the range of 5.2–5.7 eV Å^{-2} (0.8–0.9 mdyn Å^{-1}). This result shows a higher stiffness of the octahedral environment [NiO_6] than the sublattice containing Pr, as a result of the strong covalent bonding between Ni and O ions. A more precise evaluation of the Pr sublattice would be performed by collecting EXAFS data at the Pr L_3-edge, which is beyond the scope of this work.

Spin–phonon coupling contributions in monoclinic $PrNiO_3$

Similar anomalous temperature-evolutions of the Debye–Waller factor $\sigma_\Gamma{}^2$ extracted from EXAFS as observed here (*i.e.*, the departure from the Einstein-like trend at 130 K) have been reported in orthoferrite at the temperature induced magnetic ordering transition and at critical temperatures for layered superconductors. $DyFeO_3$ orthoferrite has the same orthorhombic crystal structure (*Pbnm*) of $PrNiO_3$ under room conditions.[31] This orthoferrite is a magnetic system with a spin reorientation transition (SRT) in the range of 50–100 K. Panchwanee *et al.* reported a slight compression of the bond Fe–O above SRT and an anomaly in $\sigma_\Gamma{}^2$ similar to that seen for the bond Ni–O in $PrNiO_3$ at magnetic ordering temperature $T_N \approx 130$ K, the anomaly being absent in the paramagnetic $YFeO_3$ orthoferrite. To our knowledge, both results showing the sensitivity of the EXAFS Debye–Waller factors to magnetic transitions are novel. Other prominent examples are the iron-based superconductors, as the case of $Li_x(NH_3)_yFe_2Se_2$[32] or $Ba(Fe_{1-x}Co_x)_2As_2$[33] that shows only slight bond-distance changes with temperature for the pair-unit Fe–Fe, but its associated Debye–Waller factor has a sharp and well-defined drop at T_C. For the superconductor based on $La_{1.85}Sr_{0.15}CuO_4$, two paths of Cu–O were considered to describe the planar [CuO_4] unit, where both bond-distance and Debye–Waller factor depicted anomalies at the onset of the critical temperature.[34]

In contrast to the view EXAFS studies reporting vibrational anomalies at the onset of the magnetic transitions, these anomalies have been widely reported from vibrational spectroscopy, including Raman and infrared techniques.[12,35,36] For instance, Granado *et al.* probed the temperature dependence of the Raman modes around the magnetic ordering temperatures in doped and undoped $La_{1-x}Mn_xO_3$ perovskite manganites, showing a well-distinguished softening below T_N of the stretching mode of the [MnO_6] units.[12] These results were extended for different members of the manganite family, including $RMnO_3$ (R = Pr, Nd, Sm, Eu, Gd, Tb, Dy, Ho, Y), where the role of the R cation size was established for the phonon softening behaviour: this effect is almost negligible for small R cations.[23] Since the Pr atom has an intermediate cation size among the rare-earth elements, the softening was quite evident below T_N. Later, this phonon anomaly at the onset of the magnetic ordering temperature was reported in different systems. Rodrigues *et al.* showed that this phonon softening also occurs in Ising-like spin-glasses (*i.e.* a system with short-range magnetic order), as the case of Fe_2TiO_5, using low-temperature Raman data.[37] Calder *et al.* reported a large softening of the symmetric stretching in 5d $NaOsO_3$ osmate, which was the largest shift (≈ 40 cm^{-1}) already recorded in the literature.[38] Radionov *et al.* detected an anomalous behaviour at the magnetic ordering temperature in the magnetoelectric $LiNiPO_4$ single-crystals using polarized infrared reflectance.[39] A recent paper on $RNiO_3$ nickelates (R = Y, Er, Ho, Dy, Sm, Nd) revealed phonon anomalies around both magnetic ordering and insulator-metal transition temperatures by means of Raman spectroscopy.[7]

In all of the papers mentioned above and others cited elsewhere,[40–42] the phonon anomaly is in general explained by considering the contribution of four physical effects: (i) lattice expansion/contraction described by the volume change and Grüneisen parameter; (ii) intrinsic anharmonicity of the phonon mode according to the Balkanski's model;[43] (iii) phonon renormalization due to the electronic states at the spin ordering temperature; and (iv) modulation of the exchange integral as a consequence of the spin–phonon coupling. The latter effect may be stronger when the magnetic ordering appears concomitantly with the insulator–metal transition, being the case of both $PrNiO_3$ and $NaOsO_3$. In $PrNiO_3$, one may expect that all four effects could occur, because the structural phase transition, magnetic ordering, and insulator–metal transition take place at $T \approx 130$ K.[6] In contrast to $PrNiO_3$, systems that exhibit neither concomitant structural transition nor magnetic ordering, only intrinsic anharmonicity is seen by Raman or infrared spectroscopies.[43,44] This suggests that phonon anomalies can be modelled as a first-order perturbation from the expected phonon anharmonicity. Based on this assumption and to account for any of the four physical effects mentioned above, one may propose a perturbative term ($\Delta\theta_E$) on the Einstein temperature and a modified equation of the Einstein's model:

$$\sigma_\Gamma{}^2(T;\theta_E+\Delta\theta_E,\sigma_{stat}) = \sigma_{stat}{}^2 + \frac{\hbar^2}{2\mu k_B\theta_E}\coth\left(\frac{\theta_E}{2T}\right) + \left(\frac{\partial\sigma_\Gamma{}^2}{\partial\theta_E}\right)\Delta\theta_E \quad (3)$$

where, $\Delta\theta_E$ contains four terms, such as $(\Delta\theta_E)_{latt} + (\Delta\theta_E)_{anh} + (\Delta\theta_E)_{ren} + (\Delta\theta_E)_{sp\text{-}ph}$.

The quantity $\Delta\theta_E$ can be extracted from the experimental data in Fig. 4 by estimating the difference $\sigma_\Gamma{}^2(T;\Delta\theta_E+\theta_E,\sigma_{stat}) - \sigma_\Gamma{}^2(T;\theta_E,\sigma_{stat})$ and the first-order derivative the non-perturbated Einstein's model $\left(\frac{\partial\sigma_\Gamma{}^2}{\partial\theta_E}\right)$. The former data extraction was performed using a Python-SciPy code using the method *interpolate* (linear procedure), while the latter depends on the non-perturbated Einstein temperature that is the same value obtained by Einstein's model for $T > T_N$. We have obtained the quantity $\Delta\theta_E$ from the Debye–Waller factors only for the shells Ni_a–O_a ($\Gamma_{1,2}$). Some assumptions can be considered, as follows: (i) contributions from the bond-distances Ni–O and, consequently, their anharmonicities were disregarded in the temperature range of 10–200 K, meaning that $\Delta\theta_E$ only departs from a constant value of $\theta_E = 553(2)$ K. Indeed, the anharmonic effects

take place at temperatures above 200–300 K in most of the known compounds, including oxides; (ii) $PrNiO_3$ seems to present a common mechanism for both T_N and T_{IM}, meaning that the renormalization of the electronic states is intimately connected to the modulation of the exchange integral J_{ij}. Then, the perturbation $\Delta\theta_E$ may be estimated by the term $(\Delta\theta_E)_{sp-ph}$ that is dependent on the scalar spin correlation function $\langle\vec{S}_i\cdot\vec{S}_j\rangle$, *i.e.*

$$(\Delta\theta_E)_{sp\text{-}ph} = \lambda^*\left\langle\vec{S}_i\cdot\vec{S}_j\right\rangle = \frac{\hbar^2}{2\mu k_B{}^2\theta_E} \times \sum_{i,j>i}\left(\frac{\partial^2 J_{ij}}{\partial u^2}\right)\left\langle\vec{S}_i\cdot\vec{S}_j\right\rangle \quad (4)$$

where, θ_E is the non-perturbed Einstein temperature; λ^* is the coupling constant; and J_{ij} is the exchange integral between ith and jth magnetic nickel ions.[45,46] Here, we can employ the mechanism proposed by Granado *et al.* for undoped $LaMnO_3$ which is described by the same orthorhombic space-group of $PrNiO_3$.[12] In such a mechanism, the summation of eqn 4 was evaluated along the stretching mode of the distorted $[MnO_6]$ units that contains four equatorial and two apical oxygens around the Mn cation, which can be extrapolated to the case of the $[NiO_6]$ octahedra in $PrNiO_3$, leading to the following approximation:

$$(\Delta\theta_E)_{sp\text{-}ph} \approx -\frac{2\hbar^2}{\mu k_B{}^2\theta_E}\left(\frac{\partial^2 J_{FM}}{\partial u^2}\right)\left[\frac{M_{sub}(T)}{M_0}\right]^2 \quad (5)$$

where, J_{FM} is the exchange integral evaluated at the plane that has ferromagnetic coupling, while the magnetic coupling is antiferromagnetic along orthogonal direction; $M_{sub}(T)$ denotes the sublattice magnetization per Ni^{3+} ion (staggered).

In Fig. 5, we show (a) the extracted quantity $\theta_E + \Delta\theta_E$ together with (b) the average magnetization of Ni^{3+} (μ_{Ni}) in $PrNiO_3$ from neutron diffraction in Gawryluk *et al.*,[6] (c) the first-derivative of the DC magnetic susceptibility (M/H) under heating in a magnetic field of 100 Oe, and (d) the resistivity measurements in Mroginski *et al.*[26] For the sake of comparison, Fig. 5b also has the average magnetization of Ni^{3+} in $LuNiO_3$ from the neutron diffraction data.[47] The magnetic susceptibility exhibits a strong paramagnetic signal from Pr^{3+}; however, the magnetic ordering temperature in $PrNiO_3$ is clearly seen in $\frac{d(M/H)}{dT}$ at $T_N \approx 125$ K. This value agrees with the insulator–metal transition temperature at 125 K as obtained from electrical resistivity data, then it corroborates that $T_N = T_{IM}$. The magnetization μ_{Ni} is indeed quite similar to the extracted $(\Delta\theta_E)_{sp\text{-}ph}$, *i.e.* the quadratic scaling between those quantities is consistent with eqn (5). The magnetization μ_{Ni} of $LuNiO_3$ with $T_N \approx 125$ K also scales well to the quantity $\Delta\theta_E$. Both observations strongly suggest that the anomaly seen in $\sigma_\Gamma{}^2$ is related to a spin–phonon interaction. Physically, such a phenomenon takes place when the active vibrational modes are affected by an interaction among the magnetic ions within the crystal structure, as shown in eqn (4). Beyond this finding, we obtained a value for the second-order derivative $\left(\frac{\partial^2 J_{FM}}{\partial u^2}\right)$ of $\approx$13 mRy Å^{-2}, that is close to the one reported for undoped $LaMnO_3$ ($\approx$ 16 mRy Å^{-2}).[12] This result demonstrates that the parameter $\sigma_\Gamma{}^2$ for the shells Ni_a–O_a ($\Gamma_{1,2}$) represents the stretching modes, which only involve oxygen displacements, while the central atom (Ni or Mn) is fixed when they are Raman-active modes.

In the following, we discuss the likelihood of spin–phonon coupling in $PrNiO_3$ based on the magnetic structure and the phonons. The magnetic moment of Ni arises from a collinear magnetic structure (S.G. $P2_1/n$) with two Ni magnetic moments at distinct Wyckoff sites. The magnetic propagation vector, as derived from neutron diffraction, was found to be $\vec{k} = \left(\frac{1}{2}, 0, \frac{1}{2}\right)$ and the spin operator may be projected along both *a*- and *c*-axes.[47,48] For the vibrational modes mainly concerning the stretching modes of the apical (O1; parallel to *c*-axis) and equatorial (O2; *ab*-plane) oxygens, one may expect a stronger coupling between the magnetic propagation vector for Ni ions and the eigenvectors which describe the normal modes. Therefore, this effect is seen through the softening of the Einstein temperature below T_N, as predicted by eqn (5).

The Ni K-edge EXAFS data of $PrNiO_3$ across $T_N \approx 130$ K unveiled a new ingredient for describing its itinerant behaviour, which is the spin–phonon coupling. Our results establish the role of the lattice dynamics together with orbital overlapping between Ni 3d and O 2p for describing the insulator-metal transition in $PrNiO_3$ nickelate. Additional EXAFS measurements on nickelates with differing R cations are required to untangle the perturbation $\Delta\theta_E$ from spin–phonon coupling and phonon renormalization due to the electronic states for drawing a complete picture of the underlying physics. It would be mandatory to probe it in other nickelates with T_N and T_{IM} well separated in the phase diagram, as in the case of R = Lu, Ho, Tl.

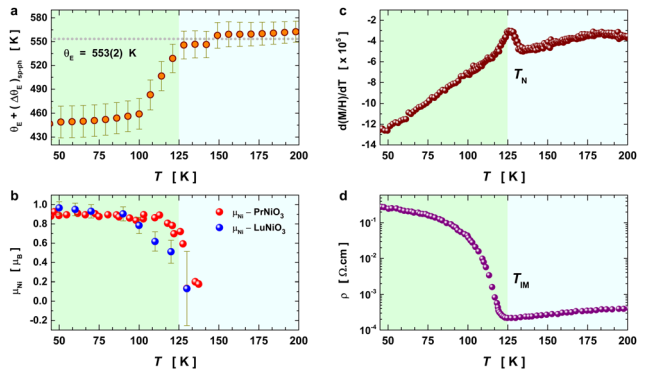

Fig. 5 Temperature variation of the Einstein temperature, staggered magnetization, magnetic susceptibility, and resistivity in $PrNiO_3$ across the IMT at $T_N \approx 130$ K. (a) Extracted quantity $\theta_E + (\Delta\theta_E)_{sp-ph}$ from the Debye–Waller factors of the first shell Ni_a–O_a ($\Gamma_{1,2}$). (b) Staggered magnetization of Ni ions in $PrNiO_3$ and $LuNiO_3$ as extracted from neutron powder diffraction.[6,47] Both compounds show magnetic transition at $T_N \approx$ 125–130 K. (c) First-derivative of the DC magnetic susceptibility (M/H) under heating in a magnetic field of 100 Oe, which display a magnetic transition at 125 K. (d) Resistivity measurements of $PrNiO_3$ as reported in Mroginski *et al.*,[26] which also exhibit the insulator–metal transition at 125 K.

Conclusions

In this work, high-purity $PrNiO_3$ nickelate has been successfully synthesized using the liquid-mixture method combined with

thermal treatments under 200 bars under an O_2 atmosphere. Synchrotron X-ray diffraction data confirmed the occurrence of the orthorhombic lattice (*Pbnm*) under room conditions, but with small impurities of NiO (<2.5% wt). Low-temperature EXAFS oscillations at Ni K-edge unveiled the very local units of the $PrNiO_3$ lattice, which were modelled in agreement with the monoclinic crystal structure ($P2_1/n$) for $T < 125$–130 K. Above this temperature, a convergence of the pair-unit distances Ni–Pr was clearly identified, denoting the stabilization of the orthorhombic lattice (*Pbnm*). The lattice dynamics of the $PrNiO_3$ nickelate across the structural transition were monitored using temperature-dependent EXAFS data in the range of 10–300 K (under isobaric conditions). From the thermal evolution of the Debye–Waller factors above 130 K, we extracted the Einstein temperatures of individual atomic pair-units and estimated the Ni–O bond stiffness. The thermal evolution of the Debye–Waller factors and bond-length evolution of the Ni–O bonds and Ni–Pr pair showed strong anomalies across the IMT. We modelled the evolution of the Ni–O bond Debye–Waller factors by means of molecular field approximation for the scalar spin correlation function. This model suggested a continuous increase of the spin–phonon coupling below the IMT transition temperature of 130 K, which was confirmed by the magnetic and vibrational properties of this compound. Our EXAFS results clearly showed that the insulator–metal transition in the $PrNiO_3$ nickelate has an important contribution from the lattice dynamics. The approach presented here may be further extended and applied to similar systems that show magnetic or insulator–metal transitions to provide a physical description of the underlying mechanisms.

Author contributions

Conceptualization, J. E. R., J. A. A., A. D. R., and O. M.; methodology, J. E. R, J. L-S., E. S-T, J. L. M., N. M. N., and O. M.; software, J. E. R.; formal analysis, J. E. R.; resources, O. M.; writing – original draft preparation, J. E. R.; writing – review and editing, J. E. R., A. D. R, J. L. M., and J. A. A; funding acquisition, J. A. A., J. L. M., and O. M. All authors have read and agreed to the published version of the manuscript.

Conflicts of interest

There are no conflicts to declare.

Acknowledgements

This research was partially funded by the Spanish Ministry of Science and Innovation, MCIN/AEI/10.13039/501100011033/, with the project numbers: PID2021-122477OB-I00, TED2021-129254B-C22, PIE: 2021-60-E-030, and PIE: 2010-6-OE-013. All the authors acknowledge the European Synchrotron (ESRF, Grenoble) for making all the facilities available for X-ray diffraction (BM25) and X-ray absorption experiments (BM23). J. E. R. thanks the anonymous reviewers for their pertinent and useful comments.

References

1 G. Catalan, *Phase Transitions*, 2008, **81**, 729–749.
2 J. Liu, E. Jia, L. Wang, K. A. Stoerzinger, H. Zhou, C. S. Tang, X. Yin, X. He, E. Bousquet, M. E. Bowden, A. T. S. Wee, S. A. Chambers and Y. Du, *Adv. Sci.*, 2019, **6**(19), 1901073.
3 E. Yadav, S. Harisankar, K. Soni and K. R. Mavani, *Vib. Spectrosc.*, 2021, **112**, 103185.
4 L. Korosec, M. Pikulski, T. Shiroka, M. Medarde, H. Luetkens, J. A. Alonso, H. R. Ott and J. Mesot, *Phys. Rev. B*, 2017, **95**, 1–5.
5 F. Serrano-Sánchez, J. L. Martínez, F. Fauth and J. A. Alonso, *Dalton Trans.*, 2021, **50**, 7085–7093.
6 D. J. Gawryluk, Y. M. Klein, T. Shang, D. Sheptyakov, L. Keller, N. Casati, P. Lacorre, M. T. Fernández-Díaz, J. Rodríguez-Carvajal and M. Medarde, *Phys. Rev. B*, 2019, **100**, 205137.
7 I. Ardizzone, J. Teyssier, I. Crassee, A. B. Kuzmenko, D. G. Mazzone, D. J. Gawryluk, M. Medarde and D. van der Marel, *Phys. Rev. Res.*, 2021, **3**, 033007.
8 M. Medarde, M. T. Fernández-Díaz and P. Lacorre, *Phys. Rev. B: Condens. Matter Mater. Phys.*, 2008, **78**, 2–5.
9 A. Y. Ramos, C. Piamonteze, H. C. N. Tolentino, N. M. Souza-Neto, O. Bunau, Y. Joly, S. Grenier, J. P. Itié, N. E. Massa, J. A. Alonso and M. J. Martinez-Lope, *Phys. Rev. B: Condens. Matter Mater. Phys.*, 2012, **85**, 1–5.
10 C. Piamonteze, in AIP Conference Proceedings, AIP, 2003, vol. 652, pp. 450–455.
11 M. Acosta-Alejandro, J. M. De León, M. Medarde, P. Lacorre, K. Konder and P. A. Montano, *Phys. Rev. B: Condens. Matter Mater. Phys.*, 2008, **77**, 1–5.
12 E. Granado, A. García, J. A. Sanjurjo, C. Rettori, I. Torriani, F. Prado, R. D. Sánchez, A. Caneiro and S. B. Oseroff, *Phys. Rev. B: Condens. Matter Mater. Phys.*, 1999, **60**, 11879–11882.
13 C. T. Chantler, X-ray absorption spectroscopy definitions, *International Tables for Crystallography*, X-ray Absorption Spectroscopy and Related Techniques, 2021, vol. I.
14 P. A. Lee, P. H. Citrin, P. Eisenberger and B. M. Kincaid, *Rev. Mod. Phys.*, 1981, **53**, 769–806.
15 J. A. Alonso, M. J. Martínez-Lope and M. A. Hidalgo, *J. Solid State Chem.*, 1995, **116**, 146–156.
16 C. Ponchut, J. M. Rigal, J. Clément, E. Papillon, A. Homs and S. Petitdemange, *J. Instrum.*, 2011, **6**, C01069.
17 S. Roobol, W. Onderwaater, J. Drnec, R. Felici and J. Frenken, *J. Appl. Crystallogr.*, 2015, **48**, 1324–1329.
18 J. Rodríguez-Carvajal, *Phys. Rev. B: Condens. Matter Mater. Phys.*, 1993, **192**, 55–69.
19 O. Mathon, A. Beteva, J. Borrel, D. Bugnazet, S. Gatla, R. Hino, I. Kantor, T. Mairs, M. Munoz, S. Pasternak, F. Perrin and S. Pascarelli, *J. Synchrotron Radiat.*, 2015, **22**, 1548–1554.
20 B. Ravel and M. Newville, *J. Synchrotron Radiat.*, 2005, **12**, 537–541.
21 B. Ravel and M. Newville, ATHENA and ARTEMIS, *International Tables for Crystallography*, X-ray Absorption Spectroscopy and Related Techniques, 2020, vol. I.
22 M. W. Lufaso and P. M. Woodward, *Acta Crystallogr., Sect. B: Struct. Sci.*, 2001, **57**, 725–738.

23 N. D. Todorov, M. V. Abrashev and V. G. Ivanov, *J. Phys.: Condens. Matter*, 2012, **24**, 175404.
24 P. Fornasini and R. Grisenti, *J. Synchrotron Radiat.*, 2015, **22**, 1242–1257.
25 G. Dalba and P. Fornasini, *J. Synchrotron Radiat.*, 1997, **4**, 243–255.
26 M. A. Mroginski, N. E. Massa, H. Salva, J. A. Alonso and M. J. Martínez-Lope, *Phys. Rev. B: Condens. Matter Mater. Phys.*, 1999, **60**, 5304–5311.
27 A. Nakatsuka, A. Yoshiasa, K. Fujiwara and O. Ohtaka, *J. Mineral. Petrol. Sci.*, 2018, **113**, 280–285.
28 J. E. F. S. Rodrigues, J. Gainza, F. Serrano-Sánchez, C. Marini, Y. Huttel, N. M. Nemes, J. L. Martínez and J. A. Alonso, *Chem. Mater.*, 2022, **34**, 1213–1224.
29 H. G. M. Edwards, *J. Mol. Struct.*, 1987, **156**, 137–142.
30 R. X. Silva, H. Reichlova, X. Marti, D. A. B. Barbosa, M. W. Lufaso, B. S. Araujo, A. P. Ayala and C. W. A. Paschoal, *J. Appl. Phys.*, 2013, **114**(19), 194102.
31 A. Panchwanee, I. Schiesaro, S. Mobilio, S. S. K. Reddy, C. Meneghini, E. Welter and V. Raghavendra Reddy, *J. Phys.: Condens. Matter*, 2019, **31**, 345403.
32 E. Paris, L. Simonelli, T. Wakita, C. Marini, J. H. Lee, W. Olszewski, K. Terashima, T. Kakuto, N. Nishimoto, T. Kimura, K. Kudo, T. Kambe, M. Nohara, T. Yokoya and N. L. Saini, *Sci. Rep.*, 2016, **6**, 1–8.
33 M. Y. Hacisalihoglu, E. Paris, B. Joseph, L. Simonelli, T. J. Sato, T. Mizokawa and N. L. Saini, *Phys. Chem. Chem. Phys.*, 2016, **18**, 9029–9035.
34 A. Bianconi, N. L. Saini, A. Lanzara, M. Missori, T. Rossetti, H. Oyanagi, H. Yamaguchi, K. Oka and T. Ito, *Phys. Rev. Lett.*, 1996, **76**, 3412–3415.
35 B. S. Araújo, A. M. Arévalo-López, C. C. Santos, J. P. Attfield, C. W. A. Paschoal and A. P. Ayala, *J. Phys. Chem. Solids*, 2021, **154**, 110044, DOI: **10.1016/j.jpcs.2021.110044**.
36 L. D. Casto, A. J. Clune, M. O. Yokosuk, J. L. Musfeldt, T. J. Williams, H. L. Zhuang, M. W. Lin, K. Xiao, R. G. Hennig, B. C. Sales, J. Q. Yan and D. Mandrus, *APL Mater.*, 2015, **3**(4), 041515.
37 J. E. F. S. Rodrigues, W. S. Rosa, M. M. Ferrer, T. R. Cunha, M. J. Moreno Zapata, J. R. Sambrano, J. L. Martínez, P. S. Pizani, J. A. Alonso, A. C. Hernandes and R. V. Gonçalves, *J. Alloys Compd.*, 2019, **799**, 563–572.
38 S. Calder, J. H. Lee, M. B. Stone, M. D. Lumsden, J. C. Lang, M. Feygenson, Z. Zhao, J. Q. Yan, Y. G. Shi, Y. S. Sun, Y. Tsujimoto, K. Yamaura and A. D. Christianson, *Nat. Commun.*, 2015, **6**, 1–6.
39 M. S. Radionov, S. A. Klimin, A. Y. Glamazda and A. V. Peschanskii, *Low Temp. Phys.*, 2022, **48**, 246–252.
40 B. S. Araújo, A. M. Arévalo-López, C. C. Santos, J. P. Attfield, C. W. A. Paschoal and A. P. Ayala, *J. Appl. Phys.*, 2020, **127**(11), 114102.
41 M. C. Weber, M. Guennou, D. M. Evans, C. Toulouse, A. Simonov, Y. Kholina, X. Ma, W. Ren, S. Cao, M. A. Carpenter, B. Dkhil, M. Fiebig and J. Kreisel, *Nat. Commun.*, 2022, **13**(1), 443.
42 J. Son, B. C. Park, C. H. Kim, H. Cho, S. Y. Kim, L. J. Sandilands, C. Sohn, J. G. Park, S. J. Moon and T. W. Noh, *npj Quantum Mater.*, 2019, **4**, 1–8.
43 M. Balkanski, R. F. Wallis and E. Haro, *Phys. Rev. B: Condens. Matter Mater. Phys.*, 1983, **28**, 1928–1934.
44 P. Fornasini, *J. Phys.: Condens. Matter*, 2001, **13**, 7859–7872.
45 W. Baltensperger and J. S. Helman, *Helv. Phys. Acta*, 1968, **41**, 668–673.
46 D. J. Lockwood and M. G. Cottam, *J. Appl. Phys.*, 1988, **64**, 5876–5878.
47 F. Serrano, M. T. Fernandez-Diaz, J. L. Martinez and J. A. Alonso, *Dalton Trans.*, 2022, **51**(6), 2278–2286.
48 J. Mesot, M. Medarde, S. Rosenkranz, P. Fischer, P. Lacorre and K. Gobrecht, *High Pressure Res.*, 1995, **14**, 35–40.